Measurement of the Amplitude and Polarization of the Electric Field by Electromagnetic Infrared Thermography

Daniel Prost

Measurement of the Amplitude and Polarization of the Electric Field by Electromagnetic Infrared Thermography

Daniel Prost

***Abstract*— The ElectroMagnetic InfraRed (EMIR) method developed and used at ONERA provides a map of the amplitude of the electric field radiated by an antenna: a thin film of low conductivity is placed in front of the EM source, the electric field induces currents which heat the film by Joule effect; this heating is measured by an infrared camera. A low-frequency modulation of the signal associated with synchronous demodulation of the images allows eliminating the parasitic thermal phenomena. By using anisotropic films with conductivity patterns, we propose here for the first time a vector measurement of the electric field. In the case of linear polarization, this technique allows to obtain the field direction, and in the case of circular polarization, to measure the axial ratio. Furthermore, we show, with the help of a patterned array, that we can obtain the spatial structure of the near field, both in amplitude and direction.**

***Index Terms*— Antenna, axial ratio, infrared thermography, near-field measurement, polarization, thin film pattern.**

I. Introduction

THE ElectroMagnetic InfraRed (EMIR) method, which has been developed by the French Aerospace Lab, ONERA, in the 90s, consists in submitting a weakly conductive thin film to an electromagnetic (EM) field. Due to induced currents, the heating of the film, proportional to the absorbed power (and therefore to the square of the field amplitude), can be recorded with an infrared camera. To increase the spatial resolution, and eliminate the effects due to thermal processes other than the local heating by the incident field (convection, conduction), the EM source is modulated at low frequency (a few Hz) while the thermal frames are being demodulated at the same frequency (lock-in thermography) [1] (see Fig. 1). This technique allows visualizing EM maps, on a large 2-D scale (thin films of 1 m^2 have been used). This method can be used for antenna radiation pattern [2], [3] measurement, or field leakage detection and in general, to rapidly obtain EM field characterization. However, using homogeneous and isotropic thin films only allows getting the (square of) amplitude of the field. This is the reason why anisotropic films have first been tested and patented by ONERA [4]. Those films are made of dielectric film partially coated with linear

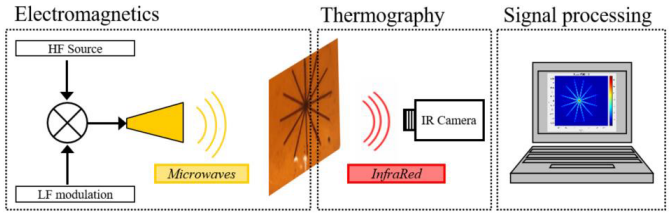

Fig. 1. EMIR method.

strips of a thin conductive layer. Such a grating does not behave like a polarizer since the electrical conductivity is weak enough but it absorbs a part of the energy of the field component parallel to the strips. Therefore, to obtain a thermal measurement, the grating had to be parallel to the field, assuming a constant linear field polarization (plane wave condition typically). Finding the direction of the field implied performing many measurements with different orientations of the grating, as in [5] and [6].

To obtain the field polarization in a general case (including circular- or elliptic-polarization), we have recently developed new films based on a specific star pattern that can directly give the field orientation (in case of linear polarization) or the axial ratio (in case of circular polarization). Moreover, by using films with such pattern-based networks, a vector mapping of the field can be obtained (especially in the case where the field structure is not that of a plane wave and exhibits a spatial variation). Although we did not measure the phase with this method, there are "plane-to-plane" (PtP) algorithms [7], [8] that can give it from two amplitude measurements at different distances from the source: the thermal measurements are processed by the PtP iterative Fourier technique to determine the phase and then the complete complex far-field pattern of an antenna for example [9]. However, these algorithms have not been tested in the case of anisotropic films. This interesting question could be addressed in future work.

II. Anisotropic Films

A. Shape and Simulations

Beyond the grating structure, we considered that a way to discriminate the direction of the electric field was to use specific patterns of lines with different directions. Simple crosses such as two lines crossing at 90° do not allow direction discrimination, since the quadratic behavior of the electric field gives two possible directions for the same components on an orthonormal basis. Therefore we focused on "star" patterns with 8 to 16 branches (see Fig. 2). The goal of such

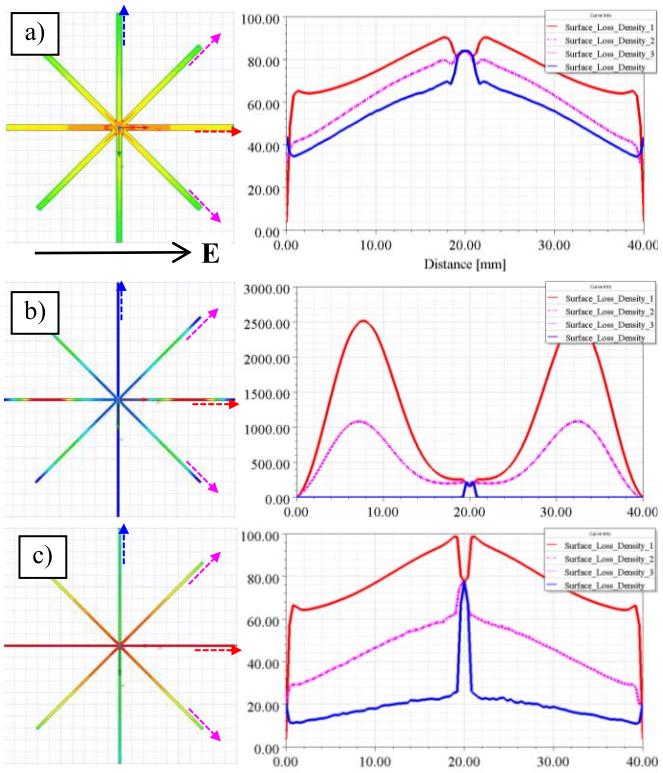

Fig. 2. |E| on star pattern and profiles along branches: (a) too wide lines leading to transverse currents, (b) too high conductivity leading to resonant behavior, and (c) optimized design.

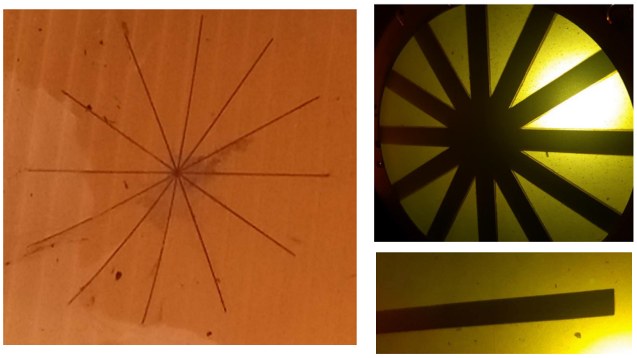

Fig. 3. Star pattern, zoomed-in view on 200-μm wide branch using a profile projector.

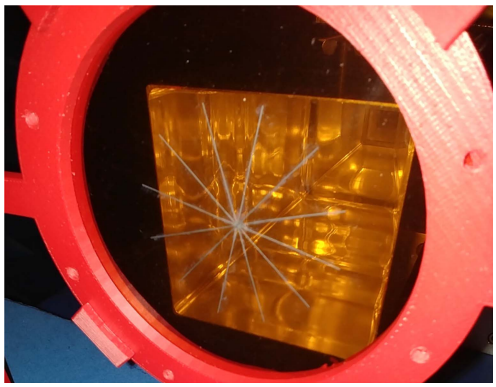

Fig. 4. Horn antenna and 12-branch patterned Kapton film.

shapes is obvious: only the branches parallel to a component of the field will heat, and the heating will be proportional to the square of the amplitude of the in-plane electric field. Resonant behavior is not expected thanks to the very weak conductivity of the pattern (with a resistance per square of almost 500 Ω). To optimize the shape and size pattern, we did some simulations (using HFSS full wave simulation software). Fig. 2 shows three cases for the surface loss density in the branches.

1) If the branches are too thick, the contrast between parallel (H) and perpendicular branches (V) to the field is not sufficient.
2) Using a too conductive pattern exhibits a resonant behavior that must be avoided (loss and heating, will be locally much too high).
3) Optimizing the surface conductivity and branch thickness provides the expected behavior: weak loss in the branches perpendicular to the field, maximum heating in the branches parallel to the field, and the same value divided by almost 2 on the 45° branches.

These simulations allowed us to converge toward an optimized design: stars with 8 or 12 branches of 200 μm width, a diameter of about 4 cm and a surface resistance of a few hundred Ohm. These rules also guided us for the etching of the samples.

B. Pattern Realization and Characteristics

The patterns are obtained by laser printing of 50-μm wide Kapton samples. The laser beam burns the Kapton locally and the resulting carbonized strips correspond to the desired pattern. Suitable laser beam parameters (power, moving celerity) are used to control the surface impedance; several passes of the beam are necessary to obtain the correct linewidth. Figs. 3 and 4 show, for example, a 12-branch star with a diameter of 5 cm. The regularity of the pattern branches is checked using a profile projector: the width is found to vary in the 200–215 μm range, which is within the required accuracy for our application.

III. Pattern and Network Structure Characterization

A. Star Pattern Performance and Management

In order to characterize the performance of the star patterns, we consider the measurement of the near field of a linearly polarized horn antenna. In this application, the star patterned film is located in front of the opening of the horn antenna. This horn antenna [10] has a square aperture and provides linear electric field polarization in the Ku-band (12–18 GHz). We voluntarily place the pattern in a "random" orientation, such that none of the branches is parallel to any side of the horn aperture (actually the orientation of the pattern does not matter, as will be shown later).

The infrared demodulated image is given in Fig. 5.

The maximum heating is obtained at the center of the star. The corresponding value is high enough to allow a quantitative measurement of the electric field amplitude. Indeed, the heating is related to the tangential electric field. Through a

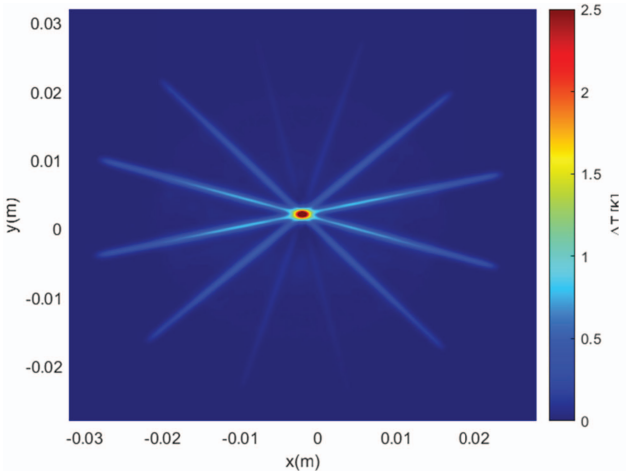

Fig. 5. Thermal image of the 12-branch star located near the horn antenna aperture.

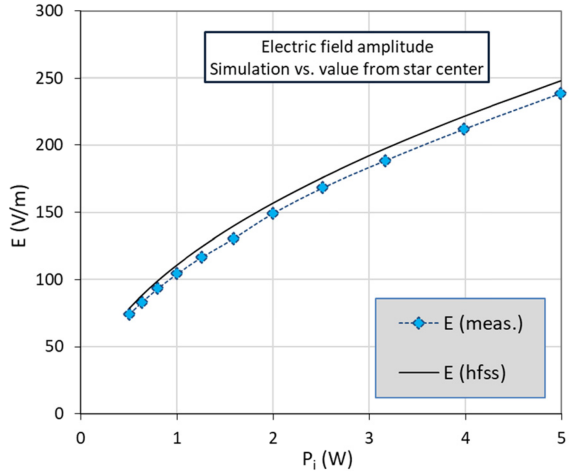

Fig. 6. Field components obtained from the thermal measurement of the 12-branch star.

thermal analysis, we can compute the absorbed surface power density, in (W/m^2) [1]

$$P_{abs} = \Delta T \sqrt{(4h^2 + (C\rho e\omega)^2)} \tag{1}$$

where

h $\approx$ 10 W/K/m^2 is the heat transfer coefficient;
$\rho = 1420$ kg/m^3 is the film density;
C $= 1090$ J/kg/K is the film heat capacity;
e $= 50$ μm is the film thickness;
$\omega = 0.5$ rad/s is the modulation low frequency.

The absorbed surface power density is also given (peak value) by

$$P_{abs} = E^2/Z_s. \tag{2}$$

Combining the two previous equations gives

$$E = k\sqrt{\Delta T}. \tag{3}$$

With our film (with surface impedance $Z_s = 200$ Ω) we obtain $k \sim 210$. N.B. This factor k can alternatively be calibrated using a reference measurement.

Moreover, as it is located in the center area of the horn aperture, we expect the pattern to give the theoretical field with maximal level. We repeated this measurement for different incident powers, from 0.5 to 5 W and compared values with HFSS simulation. Fig. 6 shows that the amplitude is correctly obtained from the heating value.

To obtain the field direction, we integrate the measured heating on each branch of the star. The integration lines are detected by matching the star pattern to the infrared image: the optimized location corresponds to the highest value of the sum of the 12 integrals. Fig. 7 represents the heating of the branches and the corresponding integration lines (the average heating $\langle \Delta T \rangle$ is given for each branch).

Taking the square roots of those heatings gives 12 components with associated angles of the electric field (Fig. 8).

One way to process those components is to consider three orthogonal bases (corresponding to the three red, blue, and green, colors in Fig. 8). On each basis, there are two possible resulting vectors for the field, since one component only gives

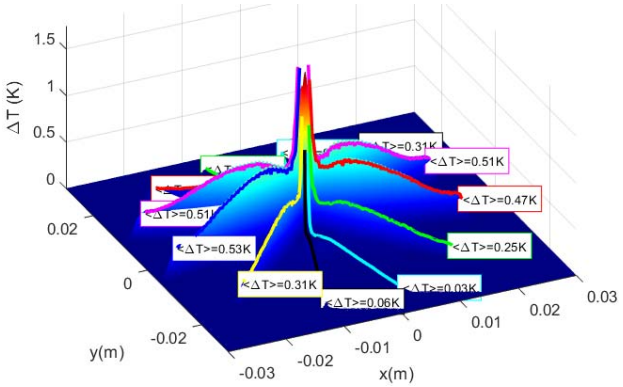

Fig. 7. E-field from IR measurement and simulation, for $P_i = 0.5$–5 W.

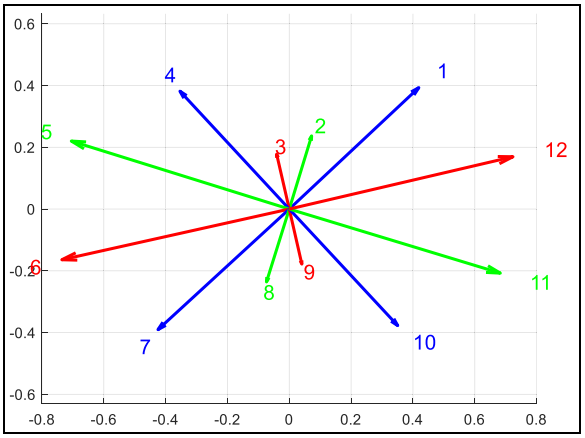

Fig. 8. Integration lines and heating along the optimized 12-branch star.

the orientation but not the direction. For instance, combining 1 and 4 (or 7 and 10) blue components from Fig. 8 gives V2 direction in Fig. 9, while combining 1 and 10 (or 4 and 7) gives V1. The same process with the green and red basis provides also two possible vectors V3 and V4 (for the green) and V5 and V6 (for the red). Finally, we obtain two possibilities for the field direction, in each of the three basis. Only one orientation is compatible with the three orthonormal bases, and corresponds to the field direction. Here only V1

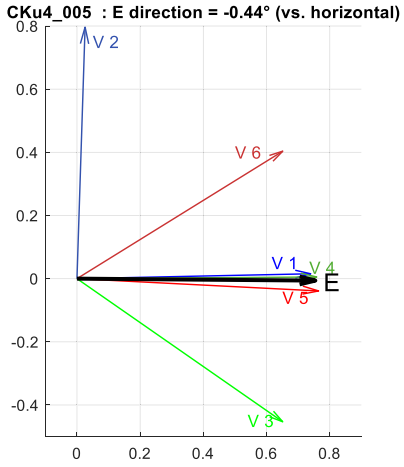

Fig. 9. Possible directions of the field in the three bases, and resulting horizontal direction detected ($f = 15$ GHz).

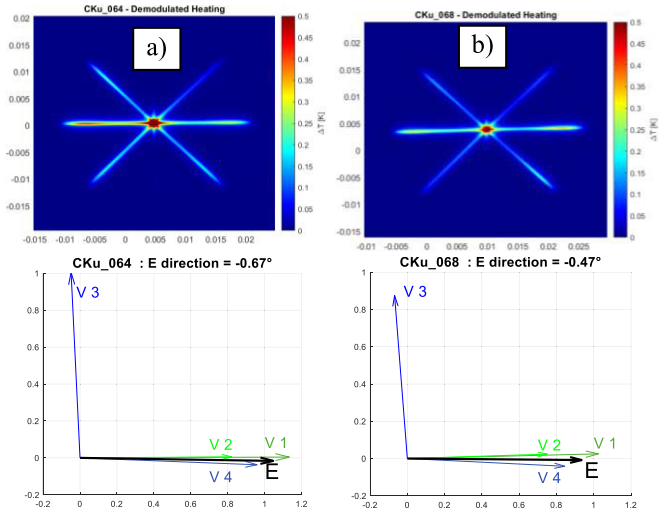

Fig. 10. (a) E-field direction given by an eight-branch star pattern and (b) second measurement on the right after applying a 1° offset angle on the film.

(from blue basis), V4 (from green), and V5 (from red) are compatible. The mean value ⟨V1, V4, V5⟩ gives the field direction ($-0.44°$ versus the horizontal axis in this case).

To check the accuracy of the detection, we duplicated this measurement with another sample with only eight branches. Moreover, we achieved two more measurements, the second one after having slightly turned the film (by almost 1°).

We obtained on Fig. 10 an angle equal to $-0.67°$ (respectively $-0.47°$) with the eight-branch star pattern (respectively after moving it slightly and rotating it by 1°). As we measured $-0.44°$ with the 12-branch star pattern, it appears that this method gives the field orientation with an accuracy better than 0.3°.

B. Star-Pattern-Based Network Performance

In this paragraph, we present another kind of film, with an array of several stars. The purpose of this array is to allow a spatial resolution of the field structure, for cases where this structure is not homogeneous (particularly when we are out of the plane wave regime). Each pattern or element of the network will provide a local measurement of the electric field.

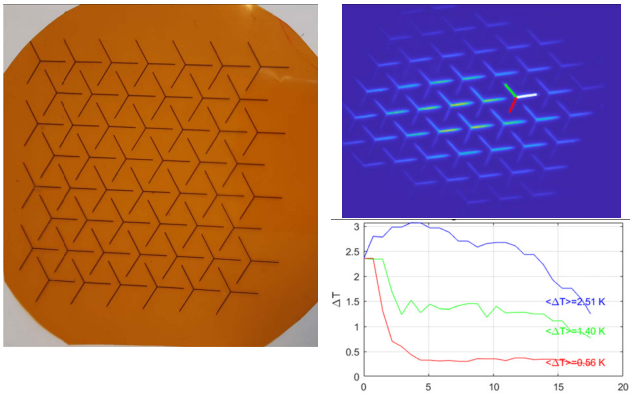

Fig. 11. Compact network of three-branch star patterns, thermal image, and three heating corresponding to one of the patterns.

Having such a network with many stars is a topology problem, since the star must be as large as possible, but the distance between two centers is as small as possible since it determines the spatial resolution. It appears that three-branch stars permit a quite compact network: for example in Fig. 11 the elements are distant of 1 cm from each other while the branches have a length of 7 mm.

The way each three-branch pattern element gives the local field direction is slightly different from the eight and 12-branch patterns presented before. Indeed, we may still define three coordinate systems, but they are not orthogonal anymore. Therefore, the measured heating on a given branch cannot directly give a field component. Let us define $\vec{e}_1$, $\vec{e}_1$, and $\vec{e}_1$, the three directions of the three branches of the star. The heating on branch $\vec{e}_1$ (respectively $\vec{e}_2$) for instance, corresponds to the square of the scalar product

$$x_1 = \vec{E}|\vec{e}_1 \text{ (respectively } x_2 = \vec{E}|\vec{e}_2). \tag{4}$$

However, here we are on a non-orthogonal basis $(\vec{e}_1, \vec{e}_2)$. The Gram-Schmidt orthogonalization process [11] is required to obtain the components on a (local) orthogonal basis; we obtain

$$\vec{x} = \begin{pmatrix} x_1 \\ x_2 \end{pmatrix} = G_{12}\vec{E}_{(\vec{e}_1,\vec{e}_2)} \quad \text{with } G_{12}\begin{pmatrix} \vec{e}_1|\vec{e}_1 & \vec{e}_2|\vec{e}_1 \\ \vec{e}_1|\vec{e}_2 & \vec{e}_2|\vec{e}_2 \end{pmatrix} \tag{5}$$

where G_{12} is the Gram-Schmidt matrix (two branches are 120° angle-shifted)

$$G_{12} = \begin{pmatrix} 1 & -1/2 \\ -1/2 & 1 \end{pmatrix} \tag{6}$$

$$\vec{E}_{(\vec{e}_1,\vec{e}_2)} = G_{12}^{-1}\vec{x}. \tag{7}$$

The last step consists of a rotation to come back in the global $(\vec{i}, \vec{j})$ reference coordinate system, which corresponds to (using the usual R rotation matrix)

$$\vec{E}_{(\vec{i},\vec{j})} = R_{12}\vec{E}_{(\vec{e}_1,\vec{e}_2)}. \tag{8}$$

This finally gives E_x and E_y components in the reference system but uncertainty still remains since two field orientations are possible

$$\vec{E}_{(\vec{i},\vec{j})} = E_x\vec{i} + E_y\vec{j} or \vec{E} = E_x\vec{i} - E_y\vec{j}. \tag{9}$$

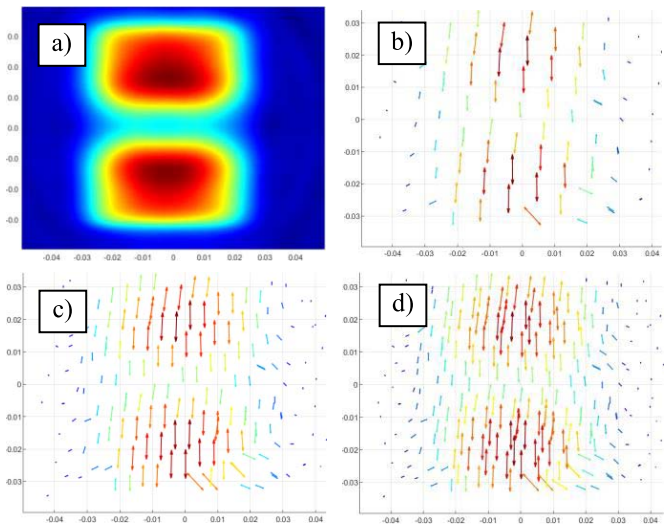

Fig. 12. Horn antenna near field: (a) amplitude "traditional" EMIR measurement [2], (b) amplitude and direction (array of three-branch stars), (c) same with two measurements collected for two films positions, and (d) three positions.

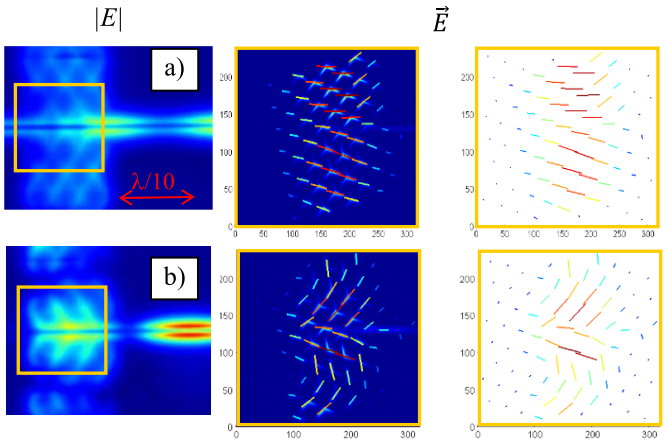

Fig. 13. HIS near electric field: direction changes with frequency: (a) operational frequency (1.4 GHz) and (b) resonant frequency (1.9 GHz).

The same process is achieved on the two other bases $(\vec{e}_2, \vec{e}_3)$ and $(\vec{e}_3, \vec{e}_1)$, with corresponding G_{23} and G_{31} Gram-Schmidt and R_{23} and R_{31} rotation matrices. Having those three solutions in the three coordinate systems makes it possible to remove the uncertainty, as in Section III-A. Fig. 12(b) illustrates for instance what can be obtained for the horn antenna of Section III-A. In order to improve the spatial resolution, we collected several measurements at different positions of the film (half a step size displacements, in H than in V direction): Fig. 12(c) and (d).

To illustrate how this array can resolve a complex electric field structure, at a much lower λ scale, we also tested it on a high impedance surface (HIS) metamaterial structure. It consists of a microstrip line with a special structure of mushrooms-type resonant elements localized inside the substrate, between the ground plane and the line [12]. This kind of structure is developed in order to reduce the size of radiating elements, in particular in the GNSS context (where Controlled Radiation Pattern Antennas–CRPAs-are often used), by limiting the coupling between the elements. To develop and study such structures, the measurement of the near electric field is necessary. Due to its small dimensions, a high spatial resolution is very hard to obtain with a standard probe measurement technique. Infrared thermography is therefore particularly interesting in this case. To this extent, in [13], infrared frames of the electric field amplitude had been obtained using the "traditional" EMIR method. With a star-patterned network film, we can now exhibit both the amplitude and the local direction of the electric field, with accurate details at a very low scale. As seen in Fig. 13, this direction changes with frequency. In particular, resonant and passing frequencies correspond to very different electric field structures.

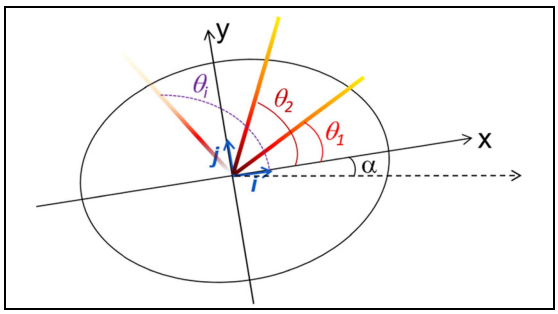

Fig. 14. Offset angle α and branch angles θ_i on a global basis.

C. Evaluation of Axial Ratio for Circular Polarization

In a circular polarized field, each branch of the star is expected to heat equivalently. However, in the very common case of imperfect circular polarization, it is of interest to estimate the axial ratio (the ratio between the major and minor axes), usually given by

$$AR = 20Log(E_x/E_y). \tag{10}$$

Let us assume an elliptical polarization of the electric field. The patterned film is located in the wave plane (perpendicular to the wave vector). In a $(\vec{i}, \vec{j})$ reference coordinate system corresponding to the orientation α of the ellipse, the electric field can be written as

$$\vec{E}_{(\vec{i},\vec{j})} = E_x(t)\vec{i} + E_y(t)\vec{j} \tag{11}$$

with $E_x(t) = E_x.sin(\omega t)$ and $E_y(t) = E_y.cos(\omega t)$.

In the same coordinate system, the direction vector of a given branch θ_i of the star is written as (see Fig. 14)

$$\vec{v_{\theta_i}} = \cos(\theta_i)\vec{i} + \sin(\theta_i)\vec{j}. \tag{12}$$

The squared scalar product gives the expected heating of the branch

$$\Delta T_{\theta_i} = \langle \vec{E} | \vec{v_{\theta_i}} \rangle^2 = (E_x(t)\vec{i} + E_y(t)\vec{j} | \cos(\theta_i)\vec{i} + \sin(\theta_i)\vec{j})^2. \tag{13}$$

Then, after integration over time, we find

$$\Delta T_{\theta_i} = E_x^2 \cos^2(\theta_i) + E_y^2 \sin^2(\theta_i). \tag{14}$$

The EMIR measurement thereby provides measurements of the heating on each branch $\Delta T_m(\theta_i)$. We thus must compare

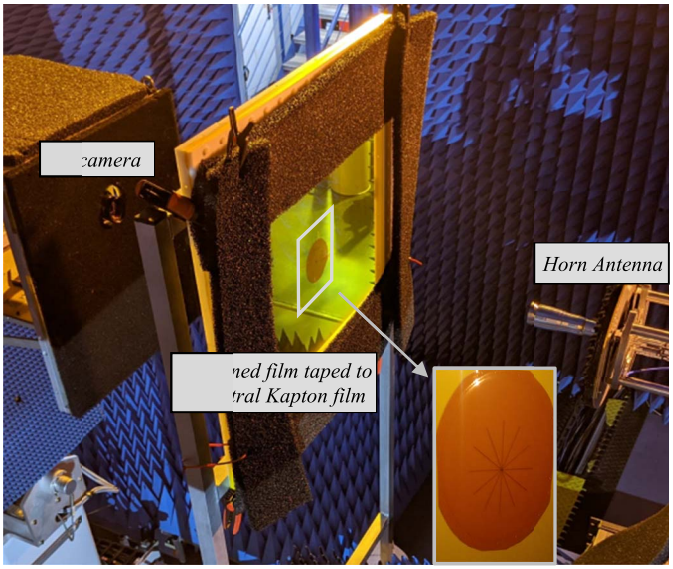

Fig. 15. 12-branch star-patterned film for circular polarization measurement.

these measurements with the computed heating figures of (14), which depend on the three unknowns (α, E_x, E_y). Placed in the actual elliptical polarization coordinate system, the following error function $\mathcal{E}(\alpha, E_x, E_y)$ must be minimum (n being the number of branches):

$$\mathcal{E}(\alpha, E_x, E_y) = \sum_{i=1}^{n} [\Delta T_m(\theta_i) - \Delta T(\theta_i)]. \qquad (15)$$

The n angles θ_i are known to be within the angular offset α, and the $\Delta T(\theta_i)$ depend also on E_x and E_y.

After having minimized this three-variables function (for instance using the MATLAB "fminsearch" function or equivalent), we obtain ellipse parameters E_x, E_y, and α, (and consequently the orientation of the ellipse and its axial ratio).

Fig. 15 shows the 12-branch star patterned film located in front of a circularly polarized Ka-band horn antenna. The camera (not visible in the picture) is behind the film. Note that the horn-to-film distance can be reduced to the far/near-field boundary. This could be useful in the case where we measure the AR as a function of angle: indeed, we only present here boresight measurements of the AR, but for many applications it is important to know how the AR depends on the angle (to obtain the AR Beamwidth). The best solution is, therefore, after having placed the film and the camera precisely in the antenna boresight angle, to rotate the antenna itself (this is much easier than moving the film and/or IR camera). Thus, the thin film and the camera sensor remain strictly parallel, and we avoid any optical distortion of the star pattern. The closer the film is, the wider the range of angles that can be explored.

The measurement at 19 GHz (middle of the band) is given in Fig. 16:

The minimization process applied to EM mapping (obtained from Fig. 16) gives the axial ratio AR = 0.19 dB (Fig. 17).

Another measurement at the very beginning of the frequency range of the antenna (f = 17.3 GHz) illustrates the degradation of the axial ratio that reaches 0.45 dB. In this case, we repeated the measurement with different powers (and a much lower horn-to-film distance). As expected (Fig. 18), the radiated power only increases the E_x and E_y values but it has obviously no impact on the orientation and axial ratio. This also proves the robustness of the measurement.

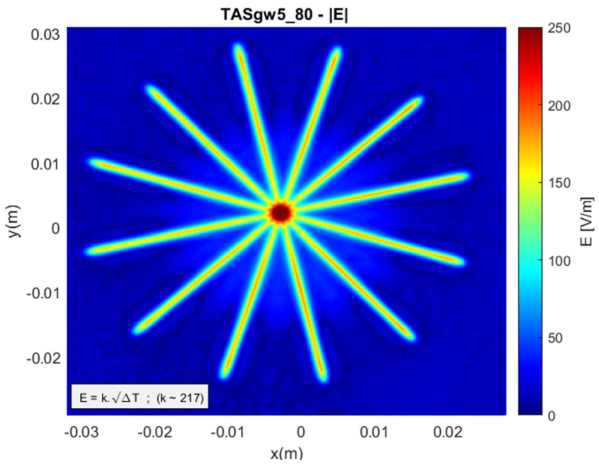

Fig. 16. Thermal (scaled and root squared) image of a 12-branch star pattern.

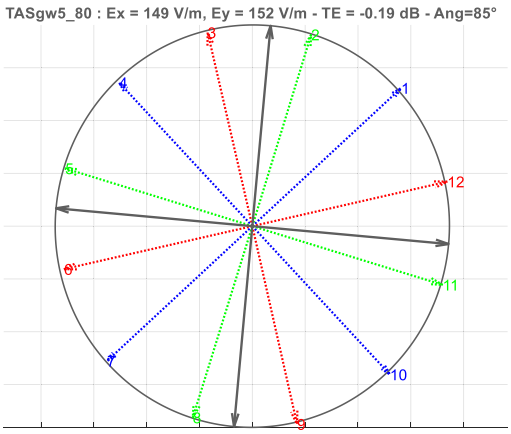

Fig. 17. Ellipse obtained from Fig. 16 measurement (f = 19 GHz).

To conclude, we compared the axial ratios obtained using this original EMIR method with traditional RF measurements, over the whole antenna band (17.5–20.5 GHz). Compared to those traditional RF techniques, the EMIR technique offers an alternative process: Fig. 19 shows a good consistency between the two methods, although an uncertainty of about 0.2% persists on EMIR measurements. This uncertainty can be attributed to several factors: 1) the limited number of camera pixels corresponding to a branch of the star pattern, which also depends on the relative position of the branch with respect to the camera frame and thus varies between branches (this problem could be solved using a higher camera resolution); 2) the widths of the branches are not strictly equal (see Section II-B), leading to under or overestimation of the heating; and 3) the tolerances of the positioning system, although extremely small (we have taken care on this), are not zero. However, the usual specification that the axial ratio should be less than 0.5 dB in the band can be validated by the EMIR method.

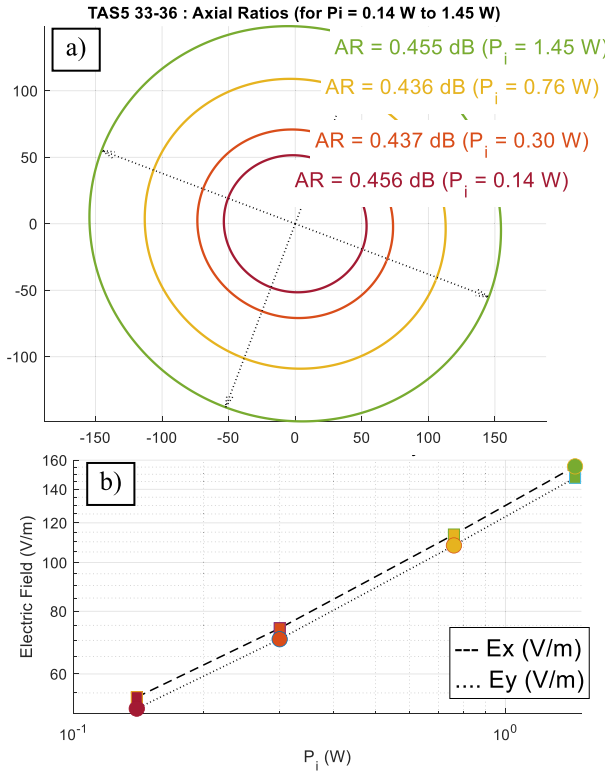

Fig. 18. (a) Ellipses and axial ratios for different powers P_i. (b) Amplitudes of E_x and E_y proportional to $\sqrt{P_i}$. ($f = 17.3$ GHz).

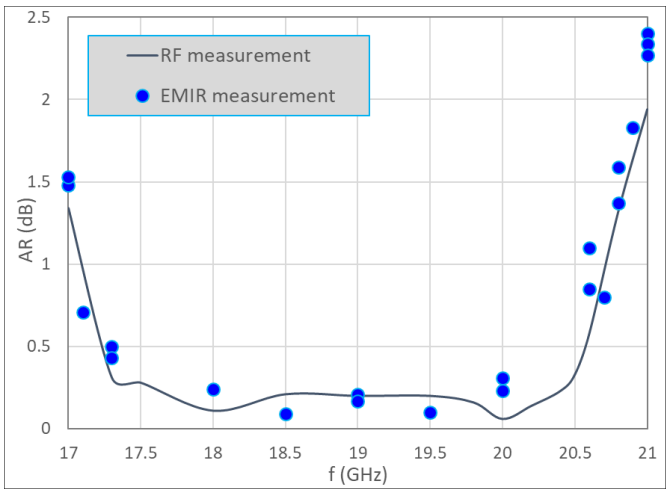

Fig. 19. Axial ratio as a function of frequency: comparison of EMIR and usual RF methods.

IV. Conclusion

Infrared thermography is now a well-proven method to obtain maps of the electric (or magnetic) field amplitude. We have shown here that it can also give the polarization of the field, i.e., its direction (for linear polarization) or its axial ratio (for circular polarization). This is achieved by placing in the wave plane an insulating thin film on which weakly conductive patterns are etched. The advantage of this method is that it is relatively easy to implement, as it requires neither a very rigorous alignment nor a perfectly controlled displacement of the sensor with respect to the radiating source. Moreover, in the case of a specific near-field structure, a network of these patterns can also reveal the spatial distribution of the field, even with details much smaller than the wavelength.

Acknowledgment

The author would like to thank Thales Alenia Space (TAS) for making available the horn antennas and providing measurement facilities. He was grateful to the CIRIMAT Lab, Center Inter-universitaire de Recherche et d'Ingénierie des Matériaux, UMR CNRS 5085, for providing the printed films that were used in this work.

References

[1] D. Balageas and P. Levesque, "EMIR: A photothermal tool for electromagnetic phenomena characterization," *Revue Générale Thermique*, vol. 37, no. 8, pp. 725–739, Sep. 1998.

[2] D. Prost, F. Issac, and M. Romier, "Imaging electric and magnetic near field of radiating structures by infrared thermography," in *Proc. Int. Symp. Electromagn. Compat. (EMC Europe)*, Barcelona, Spain, Sep. 2019, pp. 311–314.

[3] D. Prost, F. Issac, M. Romier, and D. Belot, "EMIR field imaging for diagnosis and characterization of space antennas," in *Proc. 38th ESA Antenna Workshop*. Noordwijk, The Netherlands: ESTEC, 2017, sec. 5.

[4] D. Prost and M. Romier, "Dispositif pour révéler des variations spatiales de polarisation d'un rayonnement électromagnétique," French Patent FR1910495, Mar. 26, 2021.

[5] P. Levesque and L. Leylekian, "Capteur de champ électromagnétique par thermographie infrarouge," French Patent FR9816079, Dec. 17, 1998.

[6] P. Levesque and L. D. L. et Balageas, "Vector characterization of electromagnetic fields by infrared thermography," in *Proc. 5th Quantitative InfraRed Thermography (QIRT)*, Reims, France, Jul. 2000, pp. 18–21.

[7] O. M. Bucci, C. Gennarelli, and C. Savarese, "Fast and accurate near-field-far-field transformation by sampling interpolation of plane-polar measurements," *IEEE Trans. Antennas Propag.*, vol. 39, no. 1, pp. 48–55, Jan. 1991, doi: 10.1109/8.64434.

[8] J. E. Will, J. Norgard, C. Stubenrauch, K. MacReynolds, M. Seifert, and R. Sega, "Phase measurements of electromagnetic fields using infrared imaging techniques and microwave holography," *Proc. SPIE*, vol. 2766, pp. 323–333, Mar. 1996.

[9] R. G. Yaccarino and Y. Rahmat-Samii, "Phaseless bi-polar near-field measurements using a two-plane squared amplitude interpolation algorithm," *IEEE Antennas Propag. Soc. Int. Symp.*, Jun. 1995, pp. 248–251, doi: 10.1109/APS.1995.530007.

[10] I. Albert, M. Romier, D. Belot, J.-P. Adam, and P. Hamel, "Design, manufacturing and test of a spline-profile square horn for focal array applications," in *Proc. 15 Int. Symp. Antenna Technol. Appl. Electromagn.*, Jun. 2012, pp. 1–3.

[11] Y. K. Wong, "An application of orthogonalization process to the theory of least squares," *Ann. Math. Statist.*, vol. 6, no. 2, pp. 53–75, Jun. 1935.

[12] D. Sievenpiper, L. Zhang, R. F. J. Broas, N. G. Alexopolous, and E. Yablonovitch, "High-impedance electromagnetic surfaces with a forbidden frequency band," *IEEE Trans. Microw. Theory Techn.*, vol. 47, no. 11, pp. 2059–2074, Nov. 1999.

[13] D. Prost, F. Issac, C. Martel, N. Capet, J. Sokoloff, and O. Pascal, "Electric field imaging of a high impedance surface for GNSS array decoupling application," *Eur. Phys. J. Appl. Phys.*, vol. 72, no. 1, p. 11001, Oct. 2015.

Daniel Prost received the Engineering degree from the Institut National Polytechnique de Grenoble (INPG), Grenoble, France, in 1991, and the Ph.D. degree in magnetic properties of superconductors from the Laboratoire de Physique des Solides d'Orsay (LPS), University of Paris-Sud, Orsay, France, in 1994.

He worked as a Research Engineer in different industrial companies (Schneider Electric, Schlumberger), on various subjects (circuit breakers, electric arc, magnetic sensors, simulation). In 2008, he joined the French Aerospace Lab ONERA, Toulouse, France, to work on the measurement of microwave electromagnetic fields and more particularly to develop the EMIR method in the context of the aerospace industry.